arXiv:2401.07901v1 [astro-ph.GA] 15 Jan 2024

Hunt for complex cyanides in protostellar ices with JWST

Tentative detection of CH_3CN and C_2H_5CN

P. Nazari[1], W. R. M. Rocha[2], A. E. Rubinstein[3], K. Slavicinska[1], M. G. Rachid[2,4], E. F. van Dishoeck[1,5], S. T. Megeath[6], R. Gutermuth[7], H. Tyagi[8], N. Brunken[1], M. Narang[8,9], P. Manoj[8], D. M. Watson[3], N. J. Evans II[10], S. Federman[6], J. Muzerolle Page[11], G. Anglada[12], H. Beuther[13], P. Klaassen[14], L. W. Looney[15], M. Osorio[12], T. Stanke[5], and Y.-L. Yang[16]

[1] Leiden Observatory, Leiden University, P.O. Box 9513, 2300 RA Leiden, Netherlands
e-mail: nazari@strw.leidenuniv.nl
[2] Laboratory for Astrophysics, Leiden Observatory, Universiteit Leiden, Leiden, Zuid-Holland, Netherlands
[3] University of Rochester, Rochester, NY, USA
[4] Netherlands Organization for Applied Scientific Research (TNO), 2628 CK Delft, The Netherlands
[5] Max-Planck Institut für Extraterrestrische Physik, Garching bei München, Germany
[6] University of Toledo, Toledo, OH, USA
[7] University of Massachusetts Amherst, Amherst, MA, USA
[8] Department of Astronomy and Astrophysics Tata Institute of Fundamental Research, Homi Bhabha Road, Colaba, Mumbai 400005, India
[9] Academia Sinica Institute of Astronomy & Astrophysics, 11F of Astro-Math Bldg., No.1, Sec. 4, Roosevelt Rd., Taipei 10617, Taiwan, R.O.C.
[10] Department of Astronomy, The University of Texas at Austin, 2515 Speedway, Stop C1400, Austin, Texas 78712-1205, USA
[11] Space Telescope Science Institute, 3700 San Martin Drive, Baltimore, MD 21218, USA
[12] Instituto de Astrofísica de Andalucía, CSIC, Glorieta de la Astronomía s/n, E-18008 Granada, Spain
[13] Max Planck Institute for Astronomy, Heidelberg, Baden Wuerttemberg, Germany
[14] United Kingdom Astronomy Technology Centre, Edinburgh, UK
[15] Department of Astronomy, University of Illinois, 1002 West Green St, Urbana, IL 61801, USA
[16] RIKEN Cluster for Pioneering Research, Wako-shi, Saitama, 351-0198, Japan

ABSTRACT

Nitrogen-bearing complex organic molecules have been commonly detected in the gas phase but not yet in interstellar ices. This has led to the long-standing question of whether these molecules form in the gas phase or in ices. *James Webb* Space Telescope (*JWST*) offers the sensitivity, spectral resolution, and wavelength coverage needed to detect them in ices and investigate whether their abundance ratios are similar in gas and ice. We report the first tentative detection of CH_3CN, C_2H_5CN, and the simple molecule, N_2O, based on the CN-stretch band in interstellar ices toward three (HOPS 153, HOPS 370, and IRAS 20126+4104) out of the five protostellar systems observed as part of the Investigating Protostellar Accretion (IPA) GO program with *JWST*-NIRSpec. We also provide upper limits for the two other sources with smaller luminosities in the sample. We detect OCN^- in the ices of all sources with typical CH_3CN/OCN^- ratios of around 1. Ice and gas column density ratios of the nitrogen-bearing species with respect to each other are better matched than those with respect to methanol, which are a factor of ~5 larger in the ices than the gas. We attribute the elevated ice column densities with respect to methanol to the difference in snowline locations of nitrogen-bearing molecules and of methanol, biasing the gas-phase observations toward fewer nitrogen-bearing molecules. Moreover, we find tentative evidence for enhancement of OCN^-, CH_3CN, and C_2H_5CN in warmer ices, although formation of these molecules likely starts along with methanol in the cold prestellar phase. Future surveys combining NIRSpec and MIRI, and additional laboratory spectroscopic measurements of C_2H_5CN ice, are necessary for robust detection and conclusions on the formation history of complex cyanides.

Key words. Astrochemistry – Stars: Low-mass – Stars: protostars – ISM: abundances – ISM: molecules – Techniques: spectroscopic

1. Introduction

Complex organic molecules (COM; species with ≥ 6 atoms containing carbon) are thought to be the precursors of larger species that are necessary for habitable worlds (Herbst & van Dishoeck 2009). COMs have been observed in the gas phase in various stages of star formation such as the prestellar phase (e.g., Bacmann et al. 2012; Jiménez-Serra et al. 2016), protostellar phase (e.g., van Dishoeck et al. 1995; Cazaux et al. 2003; Jørgensen et al. 2016; Lee et al. 2017; Belloche et al. 2020; van Gelder et al. 2020; Martín-Doménech et al. 2021; Nazari et al. 2021; Diaz-Rodriguez et al. 2022) and even protoplanetary disks (e.g., Öberg et al. 2015; Brunken et al. 2022). These observations have motivated many laboratory and modeling works to understand how and when COMs form (see reviews by Jørgensen et al. 2020; Ceccarelli et al. 2023).

Multiple laboratory studies argue for the formation of these species in icy dust grain mantles in either the translucent phase, cold prestellar phase or during the later warm-up phase around

the forming protostar (Öberg et al. 2009b; Meinert et al. 2016; Fedoseev et al. 2017; Muñoz Caro et al. 2019; Qasim et al. 2019; Chuang et al. 2021; Ioppolo et al. 2021; Santos et al. 2022). If formed in ices, COMs may now be directly detected in protostellar ices with the *James Webb* Space Telescope (*JWST*), while the telescopes preceding *JWST*, such as the *Infrared Space Observatory* (*ISO*) and the *Spitzer Space Telescope*, did not have the sensitivity, spectral resolution and wavelength coverage (particularly $\sim 4.4 \, \mu m$) required to securely detect COMs. Although those telescopes provided valuable information on simple species such as H_2O, CO_2, CH_4 and NH_3, they could only provide upper limits on most COMs, except for methanol (CH_3OH) which was detected (Grim et al. 1991; Gerakines et al. 1999; Boogert et al. 2000; Keane et al. 2001; Gibb et al. 2004; Öberg et al. 2008; Pontoppidan et al. 2008; Bottinelli et al. 2010; Öberg et al. 2011; Boogert et al. 2015).

If the icy grains are heated, COMs can sublimate into the gas close to the protostar and become observable to telescopes such as the Atacama Large Millimeter/submillimeter Array (ALMA) and the Northern Extended Millimeter Array (NOEMA). Once ices sublimate, gas-phase chemistry may occur to either form (larger) COMs from simple species or to alter the abundances of the sublimated COMs (Charnley et al. 1992; Herbst & van Dishoeck 2009; Barone et al. 2015; Balucani et al. 2015; Vazart et al. 2020). Many chemical models have been developed to explain formation of these species on the dust grains or in the gas phase (Garrod et al. 2008; Aikawa et al. 2008; Walsh et al. 2014; Garrod et al. 2022).

Recent ALMA and NOEMA surveys have provided valuable information on the gas-phase column density ratios of COMs in a large number of protostellar systems (e.g., Belloche et al. 2020; Yang et al. 2021; Nazari et al. 2022; Chen et al. 2023; Taniguchi et al. 2023). These works frequently show that gas-phase nitrogen- and oxygen-bearing COMs have remarkably constant column density ratios across protostellar systems with a large range of mass and luminosity (also see Coletta et al. 2020). These constant ratios are often interpreted as COM formation in similar environments, likely in the prestellar ices. However, the cold, hard evidence is to directly detect COMs in ices and compare the ice and gas abundances to search for any relation between the two.

With the launch of *JWST*, COMs in ices can be studied with the spectroscopic instruments; Mid-InfraRed Instrument (MIRI) and Near InfraRed Spectrograph (NIRSpec). Already, hints for oxygen-bearing COMs are observed in MIRI studies (Yang et al. 2022; Rocha et al. 2023) building on the *ISO* and *Spitzer* results (Schutte et al. 1999; Öberg et al. 2011). Nitrogen-bearing COMs are as important, in particular, because nitrogen contributes to forming amino acids and nucleobases required to develop habitable worlds. Yet, elemental nitrogen is a factor of ~ 5 less abundant than oxygen, making it more difficult to observe N-bearing molecules. Therefore, much less is known about the formation and evolution of N-bearing COMs in ices or in the gas. In fact, the only N-bearing COM considered in interstellar ices with *JWST* is formamide (NH_2CHO) where Slavicinska et al. (2023) used the Early Release Science program, Ice Age (McClure et al. 2023) and the guaranteed time observation program, JOYS (van Dishoeck et al. 2023) to hunt for formamide at $7.24 \, \mu m$, which was suggested previously to be in protostellar ices by Schutte et al. (1999). Even then, Slavicinska et al. (2023) could find only upper limits on formamide column density. In this paper we use *JWST*-NIRSpec to search for nitrogen-bearing COMs through their strong CN stretching band and provide the first tentative detection of N-bearing COMs in ices.

We focus on methyl cyanide (CH_3CN) and ethyl cyanide (C_2H_5CN). They have a strong vibrational transition in the $\sim 4.4 - 4.7 \, \mu m$ range. Although methyl cyanide is one of the most used tracers of the hot core phase, its formation mechanism has been debated for decades (Huntress & Mitchell 1979; Wilner et al. 1994; Walsh et al. 2014; Le Gal et al. 2019; Nazari et al. 2023b). Moreover, it is the most abundant nitrogen-bearing COM in the gas-phase (e.g., Calcutt et al. 2018; Yang et al. 2021). Therefore, if the bulk of CH_3CN were to form in ices, it is one of the few nitrogen-bearing species that could be observed by *JWST* providing important clues to its formation mechanism. Previously, Rachid et al. (2022) investigated the presence of CH_3CN in *ISO* (also see Gibb et al. 2004) and *Spitzer* spectra and found upper limits on its ice column densities. We also include C_2H_5CN in our work given that it has a transition right next to CH_3CN, so it is impossible to quantify one without the other. Furthermore, the chemistry of C_2H_5CN is thought to be related to CH_3CN (Bulak et al. 2021), and it has high gas-phase abundances with $C_2H_5CN/CH_3CN \sim 0.1$ (Nazari et al. 2022). The hunt for CH_3CN and C_2H_5CN is now facilitated by the recent laboratory studies on their spectroscopy (Moore et al. 2010; Rachid et al. 2022).

In addition, we use the column density of OCN^- ($\sim 4.6 \, \mu m$; van Broekhuizen et al. 2005) in ices as a reference species. Given that OCN^- is thought to form from HNCO (a molecule observed abundantly in the gas phase) and NH_3 in ices (Schutte et al. 1999; Novozamsky et al. 2001; Schutte & Khanna 2003; Ruaud et al. 2016), OCN^- is an ideal reference for nitrogen-bearing molecules. When ices sublimate close to the protostar, OCN^- is thought to turn back into HNCO as it sublimates into the gas (Öberg et al. 2009a). Therefore, we compare the ice column density ratios with respect to OCN^- with the gas column density ratios with respect to HNCO.

In this work we search for CH_3CN and C_2H_5CN around the protostars observed by *JWST* as part of the Investigating Protostellar Accretion (IPA; Federman et al. 2023; Narang et al. 2023) program and tentatively detect them around three protostars for the first time. We first fit a local continuum to these data, fit laboratory data to the spectra and measure the CH_3CN, C_2H_5CN and OCN^- ice column densities (Sect. 4). We then compare our column density ratios with the gas-phase ratios in Sect. 5, discuss the chemical interpretations of our findings in Sect. 6 and conclude in Sect. 7.

2. Observations and methods

2.1. Data

Here we study the five protostars observed by *JWST* NIRSpec (Bagnasco et al. 2007; Jakobsen et al. 2022; Böker et al. 2023) in the Integral Field Spectroscopy mode (IFU; Böker et al. 2022) as part of the IPA program (project ID: 1802, PI: T. Megeath). The protostellar systems observed by this program have a range of bolometric luminosities ($\sim 0.2 - 10^4 \, L_\odot$) and protostellar masses ($\sim 0.12 - 12 \, M_\odot$). They are, in order of increasing luminosity, IRAS 16253-2429 (hereafter IRAS 16253), B335-IRS (hereafter B335), HOPS 153, HOPS 370, and IRAS 20126+4104 (hereafter IRAS 20126). Table A.1 presents the bolometric luminosities and distances of the objects. Data reduction is explained in detail in Federman et al. (2023) and Narang et al. (2023); thus we give only a brief overview of the data. The objects were observed in the G395M setting (spectral resolving power R of ~ 1000) with a 4-point dither pattern, a spatial coverage of $\sim 6'' \times 6''$, and a spatial resolution of $\sim 0.2''$. The observations cover the wavelength
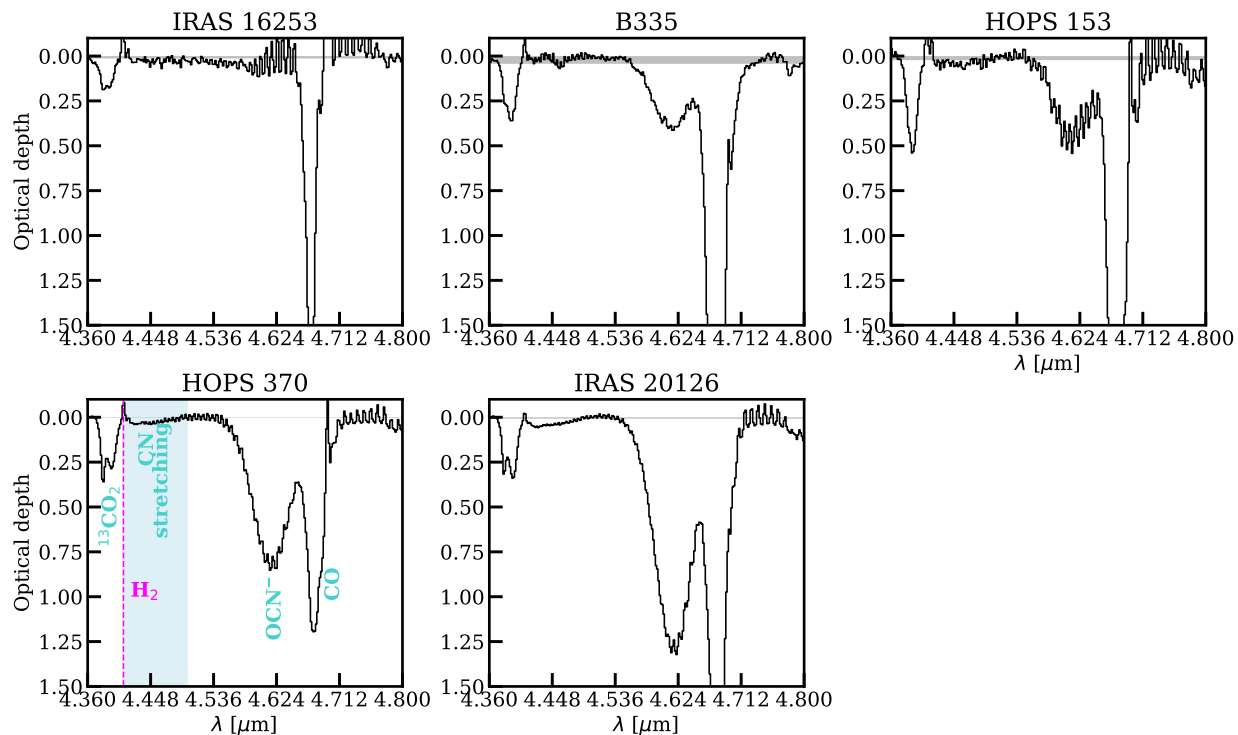
Fig. 1: Calculated optical depth for all 5 sources in the wavelength range of interest. Gray shaded area shows the optical depth 3σ uncertainty level. Although the spectra are extracted off source (see table A.1), some CO emission lines are still seen in the spectra. The CN stretching mode vibration band is shaded with light blue. The emission line between the $^{13}CO_2$ ice feature and the CN stretching band is the H_2 $0-0$ S(10) line (marked with the dashed magenta line).

range between $\sim2.87\,\mu m$ and $\sim5.27\,\mu m$. This paper focuses on the wavelength range of $\sim4.4-4.7\,\mu m$, as complex and simple species with a CN bond such as CH_3CN, C_2H_5CN, HCN, HC_3N, and OCN^- are all known to have one of their strongest transitions (the CN stretch) around this region (Soifer et al. 1979; Russo & Khanna 1996; Gibb et al. 2000; Moore et al. 2010; Rachid et al. 2022).

This work focuses on the ice features that are absorbed in the continuum, but the wavelength range of interest is also where CO rotational-vibrational gas-phase emission lines are known to lie which make the analysis of the ices more difficult (Federman et al. 2023; Rubinstein et al. 2023). Therefore, we avoided these emission lines in two ways. First, we searched the data cubes for the best spatial regions at which these gas-phase lines are less prominent. For each source we extracted the spectrum from such a region where CO emission lines are either not observed or are relatively weak. However, due to the potential remaining uncertainty by the residual gas-phase CO lines, we also analyzed the spectra extracted from the same positions using the emission-line subtracted cubes produced by Rubinstein et al. (2023). This method provided two sets of spectra with either no gas-phase emission lines or relatively weak ones which facilitated the identification of the CN stretching band.

In all cases the spectra were extracted off-source with their centers given in Table A.1 (also see Fig. A.1). The radius of the aperture (0.6″) is taken as ~3 times the full width at half maximum (FWHM) of the point spread function of NIRSpec-IFU at $4.9\,\mu m$. The rms on the continuum optical depth was calculated using the error plane of each data cube by selecting two spectral regions with least (or no) spectral features. The σ on optical depth ranges from ~0.001 to ~0.01 (see Table A.1).

2.2. Continuum determination and subtraction

The continuum was fitted locally and subsequently subtracted using the polynomial function method included in the ENIIGMA fitting tool (Rocha et al. 2021) to isolate the bands of interest from the broad water combination mode at $\sim4.45\,\mu m$. This continuum identification method has been commonly used in the literature for ice analysis (e.g., Öberg et al. 2011; Boogert et al. 2022; Slavicinska et al. 2023). Figure A.2 presents the continuum fitted to the data. We note that grain shape effects are not expected to dominate and change the ice features in our region of interest (e.g., Palumbo et al. 1995; Dartois et al. 2022). The continuum subtracted fluxes (F_λ) were then converted to optical depth through $-\ln(F_\lambda^{data}/F_\lambda^{cont})$. Figure 1 presents the continuum-subtracted spectra converted into the optical depth scale for the five sources. The 3σ on optical depth is highlighted on Fig. 1; it is larger for the lower luminosity sources.

The three most luminous sources (HOPS 153, HOPS 370, and IRAS 20126) show a significant ($S/N \gtrsim 3$) absorption feature at $4.44\,\mu m$. Continuum identification for IRAS 16253 is uncertain due to the remaining CO emission lines, hence the significance of the absorption feature at $4.44\,\mu m$ is unclear. For B335 the absorption feature is at around the 3σ level but because of the residual CO emission lines, it is difficult to conclude. Using the emission subtracted spectra the absorption feature of B335 is less than the 3σ level and thus is not significant. Hence, we focus our analysis only on the three most luminous sources.
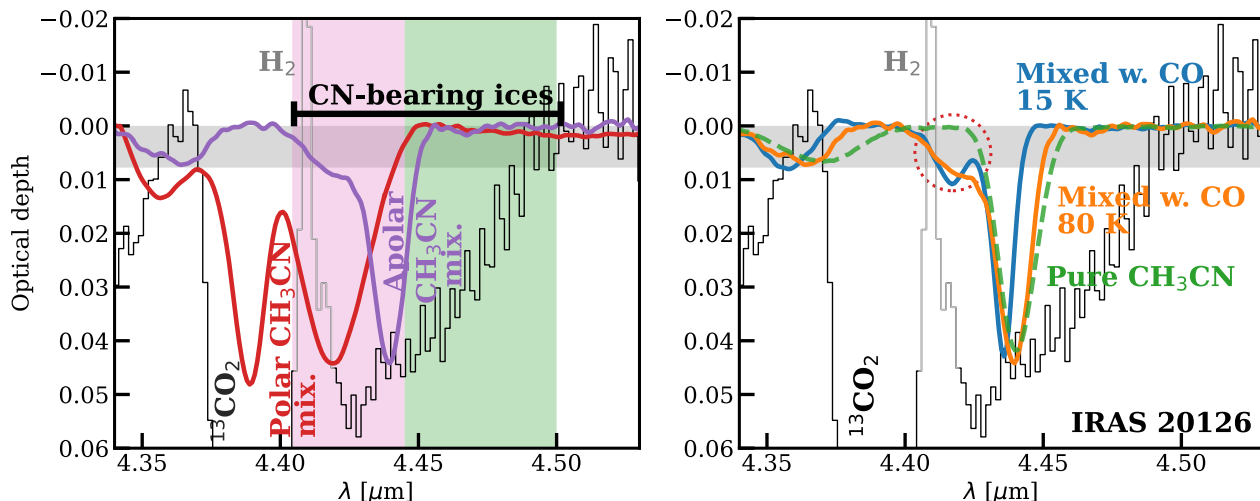
Fig. 2: Continuum subtracted spectrum of IRAS 20126 in the $4.35 - 4.5\,\mu m$ range. The shaded gray area shows the 3σ uncertainty on optical depth. The H_2 emission line at $\sim 4.41\,\mu m$ is shown in gray. *Left*: Two of the most extreme CH_3CN ice mixtures in peak position with large FWHM from Rachid et al. (2022) are shown in red and purple to demonstrate that the shaded green region cannot be explained by CH_3CN mixtures but the shaded pink region can. Red is the $CH_3CN:H_2O:CO_2$ (1:5:2, 50 K) mixture and purple is the $CH_3CN:CO$ (1:10, 80 K). *Right*: mixures of $CH_3CN:CO$ (1:10) at 15 K (blue) and 80 K (orange) to demonstrate that the one at 80 K has a larger FWHM and peak position. In addition, the red circle shows the shoulder that does not exist in the pure CH_3CN (dashed green) laboratory spectra of Rachid et al. (2022) and is produced in the CH_3CN ice feature when mixed with CO.

3. Band identification and fitting

3.1. CH_3CN

Figure 2 presents a blow-up of the 4.35-4.5 μm range for IRAS 20126, which includes the the $^{13}CO_2$ ice feature at $\leq 4.40\,\mu m$ and the CN-bearing species absorption feature at the longer wavelengths $(4.4 - 4.5\,\mu m)$. Rachid et al. (2022) considered CH_3CN infrared spectra in seven different ice mixtures and various temperatures (15-140 K). The line profiles of these various mixtures peak between $4.410\,\mu m$ up to $4.442\,\mu m$. The left panel of Fig. 2 presents two of the CH_3CN ice mixture spectra from Rachid et al. (2022) that have the shortest and longest peak wavelengths as well as a large FWHM. Figure 2 shows that although CH_3CN could be responsible for the absorption feature at $4.4 - 4.45\,\mu m$, the entire feature up to $4.5\,\mu m$ is too wide to be explained by CH_3CN mixtures alone, thus Sect. 3.2 explores other species that could be responsible for the rest of the absorption feature.

We opted for fitting the $\sim 4.40 - 4.45\,\mu m$ region with a minimum number of CH_3CN ice mixtures. We used Fig. 3 (FWHM versus peak position) and Table B.2 of Rachid et al. (2022) to carefully determine the ice mixtures that best fit the data. The minimum number of components requires features with large FWHM. The mixtures from Rachid et al. (2022) that match the absorption band at $\lambda > 4.4\,\mu m$ in peak position and have relatively large FWHM $(\sim 8 - 15\,cm^{-1})$ are $CH_3CN:CO_2$, $CH_3CN:NH_3$, $CH_3CN:CO$ (at higher temperatures) and mixtures with water. From these mixtures, those with water (polar ices) have the largest FWHM, and from those, the mixture $CH_3CN:H_2O:CO_2$ is favored to $CH_3CN:H_2O$ and $CH_3CN:H_2O:CH_4:NH_3$ because it peaks at longer wavelengths. Although favored, the mixture of $CH_3CN:H_2O:CO_2$ cannot fit the entire absorption feature thus, at least one additional component is needed to fit the $\sim 4.40 - 4.45\,\mu m$ feature.

We chose the apolar mixture $CH_3CN:CO$ as this additional component. Compared to $CH_3CN:CO_2$, $CH_3CN:CO$ at high

temperatures peaks at longer wavelengths, so it better matches the data. Between the mixtures with CO or NH_3 we opted for $CH_3CN:CO$ for two reasons: (i) the mixture with CO has a shoulder at shorter wavelengths ($\sim 4.41\,\mu m$, see right panel of Fig. 2) that avoids adding unnecessary additional components, and (ii) the CO mixture is likely more relevant for interstellar ices (Boogert et al. 2015). With $CH_3CN:H_2O:CO_2$ and $CH_3CN:CO$ the main absorption feature can be reasonably fitted, but we included the $CH_3CN:CO_2$ mixture to avoid having a dip in between the peak of $CH_3CN:H_2O:CO_2$ and $CH_3CN:CO$. Given the present uncertainties it is not possible to argue whether $CH_3CN:CO_2$ is strictly necessary to fit the absorption feature. We emphasize that our final fits (Fig. 3) are not unique and a fit can also be obtained by for example increasing the $CH_3CN:CO_2$ component and decreasing the $CH_3CN:H_2O:CO_2$ component. However the final column density of CH_3CN will only be affected by less than a factor of ~ 2.

It is not possible to constrain the temperature of the ice for $CH_3CN:CO_2$ and $CH_3CN:H_2O:CO_2$ mixtures apart from arguing that they should be below $\sim 50\,K$ and $\sim 120\,K$ under laboratory conditions, respectively, to retain the large FWHM. However, for the $CH_3CN:CO$ mixture, high temperatures ($\sim 80\,K$ as opposed to $\sim 15\,K$) better match the data by producing a larger FWHM and being centered at longer wavelengths (see right panel of Fig. 2). We note that $\sim 80\,K$ in the laboratory conditions is $\sim 30\,K$ in interstellar conditions (e.g., Boogert et al. 2015). This implies that the temperatures of ice mixtures under laboratory conditions are not equivalent to the true ice temperature in the protostellar environments because of the different time scales in those two conditions. In terms of ice morphology, this means that phase transitions and structural changes (e.g., amorphous to crystalline), would happen at higher temperatures in the laboratory. Thus, the 80 K ice mixture of CH_3CN and CO in the laboratory which still includes CO trapped in the ice is similar to a 30 K ice mixture of CH_3CN and CO in protostellar environments with most CO likely sublimated, but some trapped in

the ice. This trapping can be seen from the effect of CO on the CH_3CN absorption feature at ~4.41 μm (see the difference between CH_3CN:CO mixture and pure CH_3CN in right panel of Fig. 2).

3.2. C_2H_5CN and N_2O

There is considerable absorption (at $\gtrsim 3\sigma$) in the $4.442 < \lambda < 4.5\,\mu$m region of IRAS 20126 (see left panel of Fig. 2). Therefore, we searched the literature for other simple and complex molecules with absorption bands in this region. In total we searched for ~30 pure ices or ice mixtures at various temperatures (~10 − 150 K) to examine potential contribution from those in the ~4.4 − 4.52 μm region. We particularly used NASA's Optical Constants database[1], the Cosmic Ice Laboratory database[2] and the Leiden Ice Database for Astrochemistry (Rocha et al. 2022). This search included Oxygen-bearing species such as CH_3OCH_3, CH_3CHO and CO in addition to many nitrogen-bearing species such as HNCO and N_2O, and in particular those with a CN bond, C_2H_5CN, C_2H_3CN, C_2N_2, and HC_nN. Among the considered species, C_2H_5CN and N_2O in addition to CH_3CN were found to best match the absorption feature observed at ~4.4 − 4.52 μm. The other species did not match the data because either their peak did not match or if they had an absorption feature at the right wavelength, they showed a stronger one at a wavelength with no absorption feature in the spectrum (e.g., HCN).

To the best of our knowledge, there is no laboratory study of ethyl cyanide or N_2O ice mixtures at infrared wavelengths. Therefore, we took the pure amorphous and crystalline absorbance spectrum of N_2O at 10 K and 70 K from Gerakines & Hudson (2020). The 70 K spectrum better fit the data because its peak is at shorter wavelengths. Moreover, we took the imaginary refractive indices (k_ν) of pure laboratory measurements of amorphous C_2H_5CN at various temperatures (50-110 K) from Moore et al. (2010). Before fitting the observed spectra we converted k_ν from Moore et al. (2010) to optical depth using

$$\tau = 4\pi k_\nu \nu d, \tag{1}$$

where ν is the wavenumber and d is the ice thickness of 2.29 μm from the experiments of Moore et al. (2010). This is a first order approximation because we do not have the information on the Fresnel coefficients for these measurements.

Figure 3 presents our final model fits to the 4.4 − 4.52 μm band and the decomposition of that model into components for the five objects. We also fitted the spectra with gas-phase emission lines subtracted and the final models for those are shown in Fig. A.3. Using either the spectra before or after subtraction of emission lines we obtain only upper limits on CH_3CN and C_2H_5CN toward IRAS 16253 (due to the uncertain continuum identification) and B335. However, using both versions of the spectra we tentatively detect CH_3CN, C_2H_5CN, and N_2O toward the other three sources, all for the first time in interstellar ices.

3.3. OCN^-

The absorption feature at 4.61 μm is often referred to as the 'XCN' band and is extensively studied (Gibb et al. 2004; van Broekhuizen et al. 2005; Fraser et al. 2005; Öberg et al. 2011; Maté et al. 2012; Boogert et al. 2022). This band was suggested

---

[1] https://ocdb.smce.nasa.gov/search/ice?t=gw9anjm2av
[2] https://science.gsfc.nasa.gov/691/cosmicice/constants.html

---

by van Broekhuizen et al. (2005) to be composed of two Gaussian profiles (at 2165.7 cm^{-1} with FWHM of 26 cm^{-1} and at 2175.4 cm^{-1} with FWHM of 15 cm^{-1}). One (2165.7 cm^{-1}) can be attributed to OCN^- and the other one has been attributed to either CO bonding to grain surfaces or OCN^- in apolar ice environments (Fraser et al. 2005; Öberg et al. 2011). Moreover, the XCN band is blended with the stretching mode of CO which will affect the fitting of this region. The CO band is proposed to be composed of a Lorentzian profile (peak at 2136.5 cm^{-1} with FWHM 10.6 cm^{-1}) and two Gaussian profiles (peaks at 2139.9 cm^{-1} and 2143.7 cm^{-1} with FWHM of 3.5 cm^{-1} and 3.0 cm^{-1}) by Pontoppidan et al. (2003). Therefore, we use these line profiles in addition to the two Gaussian profiles suggested for the XCN band by van Broekhuizen et al. (2005) to fit the feature between 4.56 μm and 4.7 μm simultaneously. This method has also been used in Boogert et al. (2022) for several high-mass protostars. The fits, which match the data very well, are shown in Fig. 4.

4. Column densities

4.1. CH_3CN and C_2H_5CN

Column densities for CH_3CN and C_2H_5CN are calculated using,

$$N = \int \tau d\nu / A, \tag{2}$$

where A is the band strength, τ is the optical depth and the integral is performed in the wave number space. The measured ice column densities or upper limits are given in Table 1. The band strengths (A) used for determination of ice column densities are given in Table A.2. The band strengths for the CH_3CN ice mixtures are taken from Rachid et al. (2022) as 0.8, 0.8, and 1.75 times the band strength of pure CH_3CN (1.9×10^{-18} cm molecule^{-1}) for CH_3CN:CO_2, CH_3CN:CO and CH_3CN:H_2O:CO_2, respectively. The band strength for C_2H_5CN (50 K) is calculated as 2.86×10^{-18} cm molecule^{-1} using the following equation (e.g., Roser et al. 2021)

$$A = \frac{m}{\rho N_A} \int 4\pi \nu k_\nu d\nu, \tag{3}$$

where m is the molar mass of ethyl cyanide (55.08 g mol^{-1}), ρ is its ice density (0.703 g cm^{-3}; Gerakines et al. 2022), and N_A is the Avogadro's number. The band strength of C_2H_5CN is also determined in Gerakines et al. (2022) based on the results of Moore et al. (2010) as 2.8×10^{-18} cm molecule^{-1} which agrees well with what is found here. For the upper limits we take the maximum of the measured upper limit from the spectra before (Fig. 3) and after the emission line subtraction (Fig. A.3). The uncertainties on column densities for the tentative detections are dominated by the error in continuum fitting and the error on band strengths. The uncertainties on the band strengths are normally on the order of ~30% and those based on the choice of the continuum and the line blending are estimated as ~40%, resulting in a total uncertainty of around $\sqrt{0.3^2 + 0.4^2} = 50\%$ on the column densities. We note that the column densities measured from the spectra before (Table 1) and after subtraction of the emission lines agree within the uncertainties.
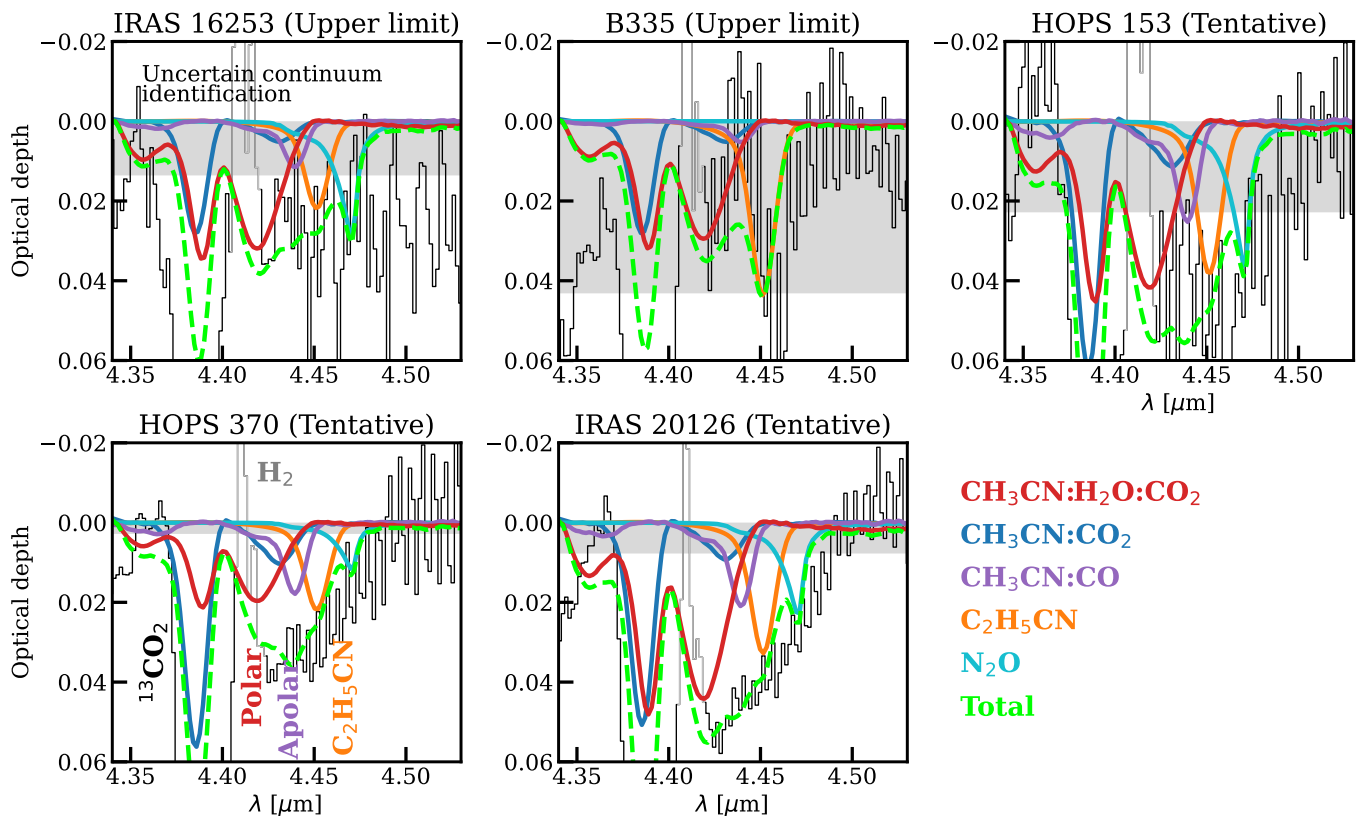
Fig. 3: Fitted CH_3CN, C_2H_5CN and N_2O models on top of the continuum subtracted data (black). The models of the various mixtures of the ice are color coded as follows, $CH_3CN:H_2O:CO_2$ (1:5:2, 50 K, red), $CH_3CN:CO_2$ (1:10, 15 K, blue), $CH_3CN:CO$ (1:10, 80 K, purple), C_2H_5CN (orange, 50 K), and N_2O (70 K, cyan). The total fit is shown with the dashed green line. The 3σ uncertainty on optical depth is shown in shaded gray. Continuum identification of IRAS 16253 is uncertain and thus the significance of the observed feature is unclear. The H_2 emission line is shown in gray and ignored when fitting (see also Fig. A.3).

Table 1: Ice column densities

Sources	N_{CH_3CN} (cm^{-2})	$N_{C_2H_5CN}$ (cm^{-2})	N_{OCN^-} (cm^{-2})
IRAS 16253	$<2.5 \times 10^{17}$	$<7.1 \times 10^{16}$	2.6×10^{16}
B335	$<2.0 \times 10^{17}$	$<1.4 \times 10^{17}$	5.0×10^{16}
HOPS 153	4.3×10^{17}	1.2×10^{17}	6.8×10^{16}
HOPS 370	2.8×10^{17}	7.1×10^{16}	1.6×10^{17}
IRAS 20126	4.0×10^{17}	1.1×10^{17}	2.6×10^{17}

Notes. The uncertainties are estimated at around 30% for OCN$^-$ and at around 50% for the other two species.

4.2. OCN$^-$

Here we are only interested in the OCN$^-$ column densities to be used as a reference for column density ratios because of its potential chemical relation to HNCO (Schutte & Khanna 2003; Öberg et al. 2009a), another molecule observed abundantly in the gas-phase (e.g., Nazari et al. 2022). Therefore, we report the column density of the red part of the XCN band (orange dashed line in Fig. 4) as the final OCN$^-$ column density. From Fig. 4 it can be seen that OCN$^-$ is detected in all sources and dominates the XCN band. We emphasize that this finding is unique to the spectra extracted from the apertures off-source as described in Sect. 2.1 (also see Fig. A.1). The ice maps of CO and OCN$^-$

found from this wavelength region are studied by Tyagi et al. (in preparation) for the IPA sources. Given the uncertainty on continuum identification of IRAS 16253, we do not analyze this object further. The band strength used for OCN$^-$ to calculate the column density is taken from van Broekhuizen et al. (2004) as 1.3×10^{-16} cm per molecule, and the column densities are presented in Table 1. The uncertainties are estimated at the ~30% level which is dominated by uncertainty on the band strength.

5. Ratios of icy cyanides and their comparison with gas-phase

Figure 5 presents the column density ratios of the considered species with respect to each other and their comparison with gas-phase observations. Our ice OCN$^-$/CH$_3$OH ratios (Fig. 5 bottom left) are consistent with the median of $0.08^{+0.16}_{-0.07}$ found for 20 sources by Boogert et al. (2022). Moreover, our tentative column densities and upper limits for CH$_3$CN/CH$_3$OH (Fig. 5 bottom middle) agree well with the average upper limits of 0.27 found in ices for four protostellar systems by Rachid et al. (2022). An intriguing finding is that the column density ratio of CH$_3$CN/OCN$^-$ in ices is around 1 (Fig. 5 top left). The main nitrogen ice carriers so far are thought to be NH$_3$ and NH$_4^+$ with a lesser contribution from OCN$^-$ (e.g., Öberg et al. 2011; Boogert et al. 2015). Although not sufficient to solve the missing nitrogen problem (Pontoppidan et al. 2014; Altwegg et al. 2019), our
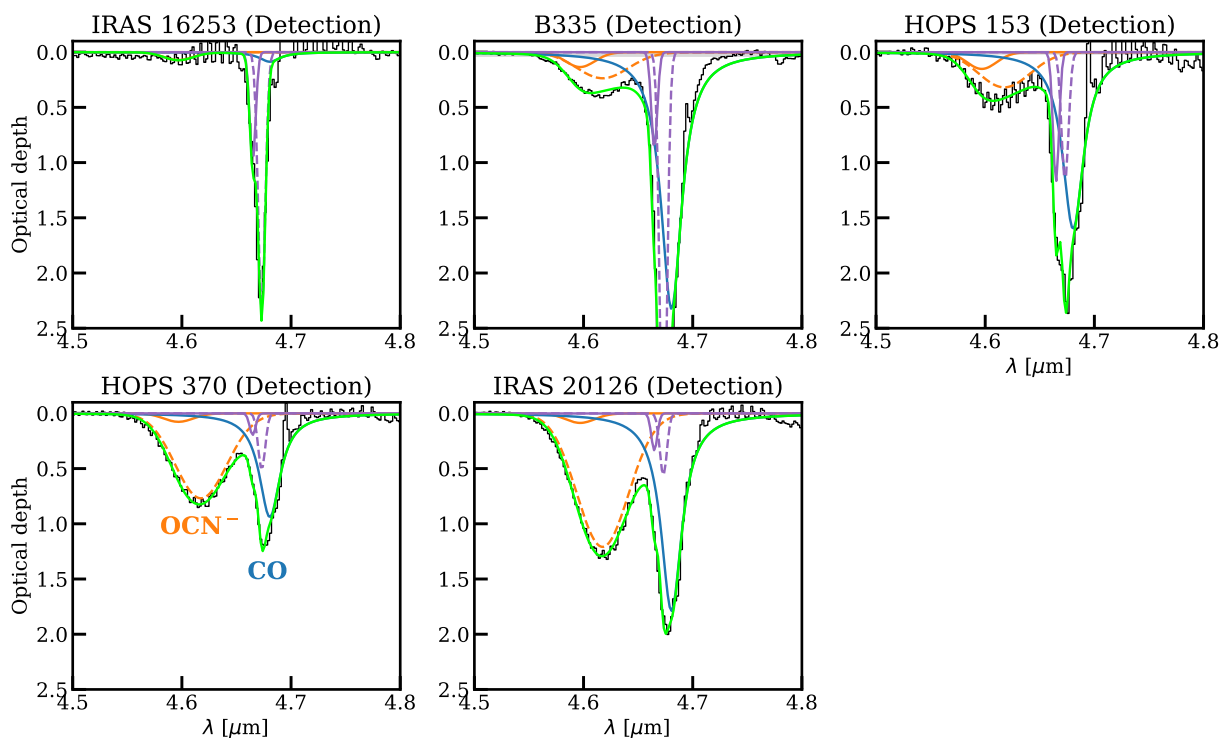
Fig. 4: Fitted model to OCN$^-$ absorption feature. Orange dashed and solid lines show the red and blue OCN$^-$ (sometimes attributed to CO absorption instead), showing that the bulk of the XCN feature is dominated by OCN$^-$. The blue and purple lines show the Lorentzian and Gaussian contributions to the CO band, respectively. The XCN and CO bands are fitted simultaneously. The total fit is shown in green. The 3σ uncertainty on optical depth is shown in shaded gray. The y-axis limit is set for better visibility of the ice features in all sources which cuts off the fit to the CO band in B335. The fit to the CO ice band in B335 is similar to the other sources and does not over predict the data.

results suggest that CH$_3$CN could be an important reservoir of nitrogen in the ices as well.

Comparing with comet 67P, our ice OCN$^-$/CH$_3$OH ratios agree within the uncertainties with HNCO/CH$_3$OH ratios in the comet (Fig. 5 bottom left). However, for CH$_3$CN/OCN$^-$ (top left) and CH$_3$CN/CH$_3$OH (bottom middle) our ice ratios are a factor of $\gtrsim 2$ larger than the comet values of CH$_3$CN/HNCO and CH$_3$CN/CH$_3$OH. Given the uncertainties, the significance of this difference is unclear.

Comparing with the gas-phase abundances, our ice ratios in the top row of Fig. 5 show a better agreement with gas-phase abundances than those in the bottom row. The tentative ice ratios of C$_2$H$_5$CN/CH$_3$CN (top right of Fig. 5) for our three sources are in particularly good agreement with the gas-phase observations at a ratio of ∼0.1. This could highlight their similar origin and formation through connected chemical formation pathways. The ratios with respect to methanol (bottom row of Fig. 5), OCN$^-$/CH$_3$OH, CH$_3$CN/CH$_3$OH, and C$_2$H$_5$CN/CH$_3$OH, show a large difference between the gas and ice (around a factor of 5 and up to a factor of ∼20).

These differences could be due to chemical effects, physical effects, or a combination of both. From a chemical perspective, given that the ratios with methanol seem to be most different, the chemistry of gas-phase methanol may require further study. For OCN$^-$/CH$_3$OH, we have assumed that all of OCN$^-$ turns into HNCO (Öberg et al. 2009a), however, it is possible that not all the OCN$^-$ in ices turns into gas-phase HNCO. For example, the efficiency of conversion of OCN$^-$ to HNCO was not clear in the lab experiments of Jiménez-Escobar et al. (2014). Another

possibility is that OCN$^-$ could be trapped in ammonium salts as suggested to exist on comet 67P (Poch et al. 2020). Based on laboratory experiments those salts will then desorb at higher temperatures than methanol (∼200 K under laboratory conditions) and during the desorption these salts can decompose into HNCO and other species (Ligterink et al. 2018). This difference in sublimation temperatures of OCN$^-$ and CH$_3$OH can affect the column density ratios as explained further in the following paragraph.

In terms of physical effects, Nazari et al. (2021) showed that if two molecules have different sublimation temperatures (different snowline locations), the gas column density ratios will not represent the true ice abundance ratios (see their Sect. 4.3). This is because normally a single source size is assumed for all compact species when calculating the column densities in unresolved gas-phase protostellar observations (e.g., Jørgensen et al. 2018; Yang et al. 2021; van Gelder et al. 2022). Therefore, a correction factor is needed to be multiplied by the gas-phase column density ratios which can be as large as a factor of ∼10 if the two molecules in the ratio have sufficiently different sublimation temperatures (e.g., CH$_3$OH, ∼100 K, and NH$_2$CHO, ∼300 K, also see Fig. 5 in Nazari et al. 2023a). The binding energies and sublimation temperatures of CH$_3$CN, C$_2$H$_5$CN, and CH$_3$OH in the amorphous water ice matrix are similar (T_{sub}∼100 K; Penteado et al. 2017; Minissale et al. 2022; Ligterink & Minissale 2023), so the correction factor is negligible. However, if these molecules are part of a different ice matrix the binding energies change. Thus a more direct measurement of the temperature that they trace is based on the excitation temperatures (T_{ex}) of the gas phase observations. The T_{ex} for the bulk of gas-phase obser-
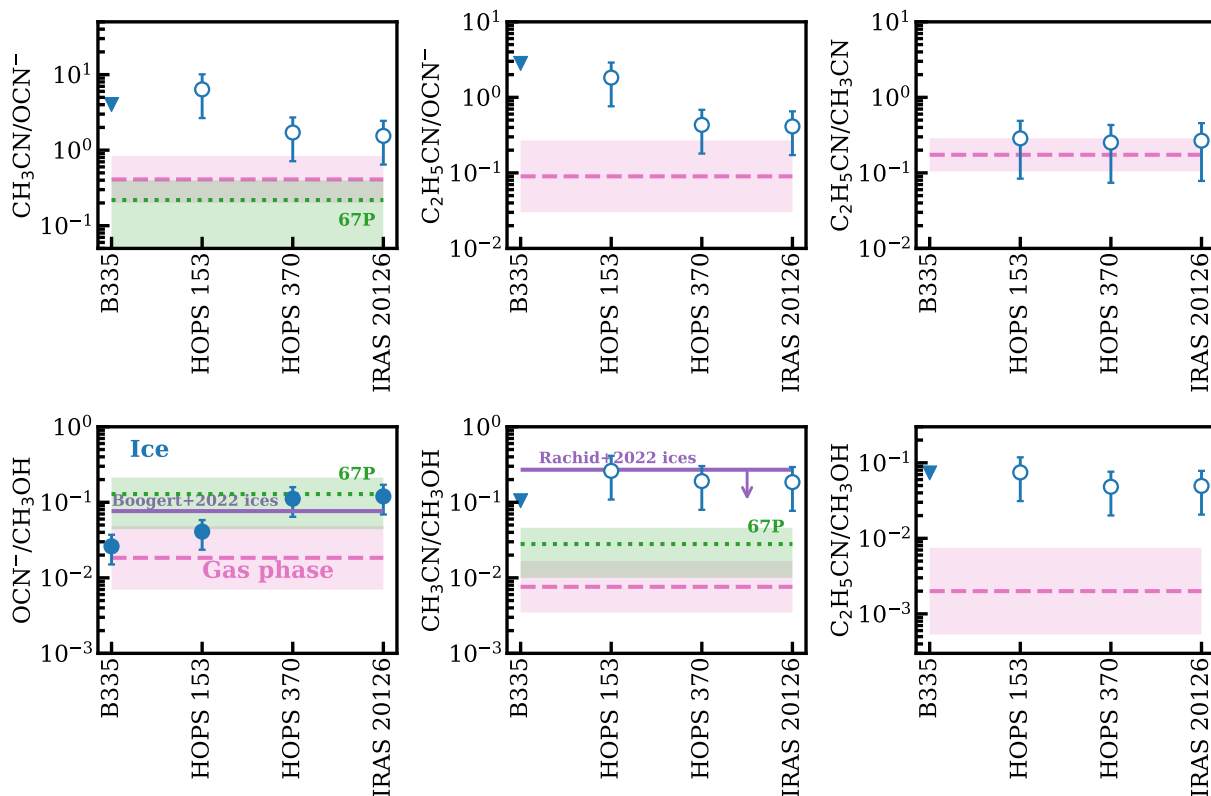
Fig. 5: Ice column density ratios (blue data points) of the species studied in the this work with respect to each other and methanol taken from Slavicinska et al. (in preparation). Filled circles show firm detections, empty ones present the tentative column densities, and filled triangles show the upper limit values. The gas-phase column density ratios of many sources from the literature are shown in the pink shaded areas (the mean and standard deviation are taken from Nazari et al. 2022). Here for the gas-phase observations we substitute OCN^- by HNCO because OCN^- is thought to turn into HNCO once sublimated. The purple lines show the previously measured ice column density ratios (median of values from Boogert et al. 2022) or upper limits (Rachid et al. 2022) in other sources. The abundance ratios of CH_3CN/CH_3OH, $CH_3CN/HNCO$, and $HNCO/CH_3OH$ for comet 67P are also shown in green (Rubin et al. 2019). See Fig. A.4 for similar plots, but corrected for potential differences in emitting areas of the N-bearing species and methanol.

vations in Fig. 5 (pink shaded area) for CH_3CN and HNCO is around 150 K while for methanol it is around 100 K (Fig. 6 of Nazari et al. 2022). Hence the correction factor to be applied to the gas-phase observations with respect to methanol is expected to be $(150/100)^{3.75} = 4.6$ based on a spherical toy model (see Eq. 4 in Nazari et al. 2021).

Including a correction factor of 4.6 in the gas-phase abundances of the bottom row (see Fig. A.4) results in the gas-phase observations of OCN^-/CH_3OH matching the ice observations within a factor of a few. Moreover, the gas-phase observations of CH_3CN/CH_3OH and OCN^-/CH_3OH, which previously did not match the comet 67P ratios of CH_3CN/CH_3OH and $HNCO/CH_3OH$, now match the comet ratios (Rubin et al. 2019). Considering the uncertainties and the small sample size it is not possible to argue whether there is still a difference between the gas and ice observations of CH_3CN and C_2H_5CN ratios with respect to methanol. We conclude that when the physical effects are considered, the ice- and gas-phase observations are in much closer agreement with each other.

Finally, to confirm the detection and column density measurements of this work (i.e., detection of at least two ice bands for each molecule), both NIRSpec and MIRI data of these sources should be analyzed in the future. Figure A.5 presents the laboratory spectrum of pure CH_3CN and C_2H_5CN in the $2.5 - 12.5\,\mu m$ regime. We note the CH_3CN feature at $3.33\,\mu m$,

which has a smaller band strength than the feature analyzed here, falls in the bulk stretch of the H_2O ice band and thus is challenging to detect. After the strongest feature at $4.44\,\mu m$, the next best features are in the wavelength range of MIRI ($\sim 6.8 - 7.4\,\mu m$). Those are particularly promising because of their larger FWHM and thus their larger or similar band strengths (Rachid et al. 2022). Although those features are embedded in strong ice features of other simple and complex species (Yang et al. 2022; Rocha et al. 2023), they could provide an additional constraint on the column densities of complex cyanides.

6. Chemical interpretation

6.1. Origin of complex cyanides

OCN^- is thought to start forming in the dense core phase after the CO freeze-out (see the review by Boogert et al. 2015). Because the CH_3CN:CO mixture was needed to fit the data, we speculate that CH_3CN starts forming in this same phase along with OCN^- (Fig. 6). In fact, this agrees with the constant gas-phase column density ratios of CH_3CN/CH_3OH with some low-level scatter found for a large sample of protostars by Nazari et al. (2022), which points to their formation likely in the cold prestellar phase. This interpretation also agrees with our finding that gas and ice ratios are similar to each other after correction
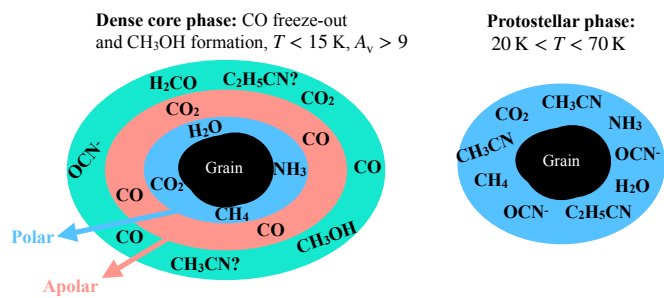
Fig. 6: Sketch of typical dust grain chemical inventory. We suggest that OCN^-, CH_3CN and C_2H_5CN likely start to form in the cold dense core phase but are enhanced thermally during the warm-up stage where more volatile species have sublimated.

Fig. 7: Column density ratios of OCN^-/CH_3OH as a function of luminosity for the IPA sources.

for source structure. The other important ice mixture explaining the data is $CH_3CN:H_2O:CO_2$, which is expected if the ices are thermally processed (see Sect. 6.2). We emphasize that the spectral fits presented here (Fig. 3) are not unique, however, mixtures of CH_3CN with CO or NH_3, CO_2 and H_2O are always needed. Because there are no laboratory spectra of C_2H_5CN ice mixtures, we cannot constrain its ice environment. The simplest assumption is that it also starts forming with OCN^- and CH_3CN in the dense core phase.

6.2. Thermal processing

Clues on the formation pathways are obtained by considering the relation between column density ratios and the bolometric luminosity. The OCN^-/CH_3OH ratios increase slightly with luminosity for our sample (Fig. 7). Additional sources are needed to confirm this relation. The OCN^- ice feature is enhanced at higher temperatures in laboratory experiments (e.g., Novozamsky et al. 2001; van Broekhuizen et al. 2004), and a potential correlation between OCN^- and luminosity is justified if the sources with higher luminosities also have higher ice temperatures with more volatile species sublimated. Brunken et al. (submitted) use spectra extracted on-source and find that IPA sources with higher bolometric luminosities also show a more prominent $^{13}CO_2$ double-peaked ice feature, which is known to indicate ice thermal processing. The locations where we extracted the spectra still show a prominent $^{13}CO_2$ double-peaked feature for IRAS 20126 and HOPS 370 (Fig. 1), while the double-peaked feature is less prominent (or non-existent) for the other sources. Therefore, ices of IRAS 20126 and HOPS 370 (the two most luminous sources in the sample) are warmer than the other sources and thus, OCN^- formation is likely enhanced (Fig. 6).

It is interesting to note that the three sources with a tentative detection of CH_3CN and C_2H_5CN are those with the highest luminosities and potentially warmest ices. Moreover, the laboratory $CH_3CN:CO$ ice mixture that fitted the data best were those at high temperatures. Hence formation of CH_3CN and C_2H_5CN might be enhanced in warmer ices. However, the non-detection in the other two sources could be simply a sensitivity problem. Therefore, a larger sample size in which these ices are detected with a range in luminosities and masses is needed to further study thermal processing of CH_3CN and C_2H_5CN in interstellar ices.

Nevertheless, this potential enhancement of CH_3CN and C_2H_5CN formation at higher temperatures is expected from their ice formation pathways. In the ice, CH_3CN is thought to
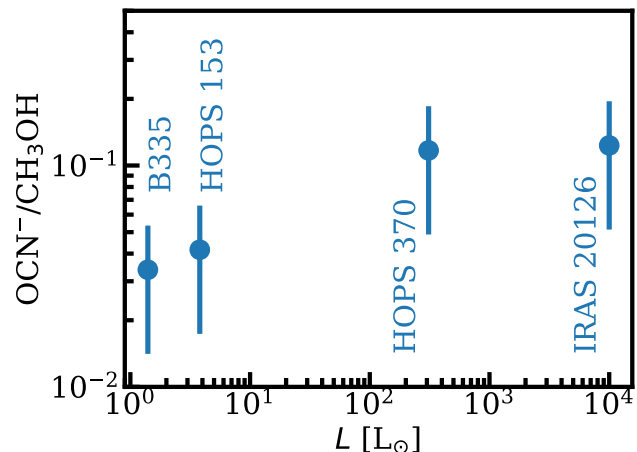
form through reaction of two radicals CH_3 and CN (Garrod et al. 2008; Garrod et al. 2022). Because ice radicals can have higher mobility at higher temperatures, CH_3CN production can increase. For C_2H_5CN, laboratory experiments using UV photolysis (Bulak et al. 2021) found that higher temperatures enhance the formation of C_2H_5CN from CH_3CN-based ices. Enhanced formation of CH_3CN and C_2H_5CN in warmer ices can also help explain the low-level scatter in the column density ratios of gas-phase observations (pink area in Fig. 5).

7. Conclusions

In this paper we report the first tentative detection of CH_3CN, C_2H_5CN, and N_2O in ices around three embedded protostars (HOPS 153, HOPS 370, and IRAS 20126+4104). Our CH_3CN/OCN^- ice ratios are on the order of 1, suggesting that CH_3CN could be a significant nitrogen reservoir in ices. Our ice column density ratios among the nitrogen-bearing species agree better between the gas and ice observations in comparison to those with respect to methanol which are around a factor of 5 larger in ices than the gas-phase. We attribute this to the difference in the snowline locations of CH_3OH and the nitrogen-bearing species studied here.

The main ice mixtures that fit the data are those where CH_3CN is mixed with H_2O, CO_2 and CO. We conclude that CH_3CN and C_2H_5CN likely start forming in the dense core phase after the CO freeze-out and could be further enhanced during the warm-up stage around the protostar.

JWST-NIRSpec data presented here help in understanding the chemistry and formation mechanism of complex cyanides. However a much larger sample of protostars with both NIRSpec and MIRI data are needed to firmly identify and statistically measure the significance of the relations proposed here.

References

Aikawa, Y., Wakelam, V., Garrod, R. T., & Herbst, E. 2008, ApJ, 674, 984
Altwegg, K., Balsiger, H., & Fuselier, S. A. 2019, ARA&A, 57, 113
Aso, Y., Kwon, W., Ohashi, N., et al. 2023, ApJ, 954, 101
Bacmann, A., Taquet, V., Faure, A., Kahane, C., & Ceccarelli, C. 2012, A&A, 541, L12
Bagnasco, G., Kolm, M., Ferruit, P., et al. 2007, in Society of Photo-Optical Instrumentation Engineers (SPIE) Conference Series, Vol. 6692, Cryogenic Optical Systems and Instruments XII, ed. J. B. Heaney & L. G. Burriesci, 66920M
Balucani, N., Ceccarelli, C., & Taquet, V. 2015, MNRAS, 449, L16
Barone, V., Latouche, C., Skouteris, D., et al. 2015, MNRAS, 453, L31
Belloche, A., Maury, A. J., Maret, S., et al. 2020, A&A, 635, A198
Böker, T., Arribas, S., Lützgendorf, N., et al. 2022, A&A, 661, A82
Böker, T., Beck, T. L., Birkmann, S. M., et al. 2023, PASP, 135, 038001
Boogert, A. C. A., Brewer, K., Brittain, A., & Emerson, K. S. 2022, ApJ, 941, 32
Boogert, A. C. A., Ehrenfreund, P., Gerakines, P. A., et al. 2000, A&A, 353, 349
Boogert, A. C. A., Gerakines, P. A., & Whittet, D. C. B. 2015, ARA&A, 53, 541
Bottinelli, S., Boogert, A. C. A., Bouwman, J., et al. 2010, ApJ, 718, 1100
Brunken, N. G. C., Booth, A. S., Leemker, M., et al. 2022, A&A, 659, A29
Bulak, M., Paardekooper, D. M., Fedoseev, G., & Linnartz, H. 2021, A&A, 647, A82
Calcutt, H., Jørgensen, J. K., Müller, H. S. P., et al. 2018, A&A, 616, A90
Cazaux, S., Tielens, A. G. G. M., Ceccarelli, C., et al. 2003, ApJ, 593, L51
Ceccarelli, C., Codella, C., Balucani, N., et al. 2023, in Astronomical Society of the Pacific Conference Series, Vol. 534, Astronomical Society of the Pacific Conference Series, ed. S. Inutsuka, Y. Aikawa, T. Muto, K. Tomida, & M. Tamura, 379
Charnley, S. B., Tielens, A. G. G. M., & Millar, T. J. 1992, ApJ, 399, L71
Chen, Y., van Gelder, M. L., Nazari, P., et al. 2023, arXiv e-prints, arXiv:2308.02688
Chuang, K. J., Fedoseev, G., Scirè, C., et al. 2021, A&A, 650, A85
Coletta, A., Fontani, F., Rivilla, V. M., et al. 2020, A&A, 641, A54
Dartois, E., Noble, J. A., Ysard, N., Demyk, K., & Chabot, M. 2022, A&A, 666, A153
Diaz-Rodriguez, A. K., Anglada, G., Blázquez-Calero, G., et al. 2022, ApJ, 930, 91
Evans, Neal J., I., Yang, Y.-L., Green, J. D., et al. 2023, ApJ, 943, 90
Federman, S., Megeath, S. T., Rubinstein, A. E., et al. 2023, arXiv e-prints, arXiv:2310.03803
Fedoseev, G., Chuang, K. J., Ioppolo, S., et al. 2017, ApJ, 842, 52
Fraser, H. J., Bisschop, S. E., Pontoppidan, K. M., Tielens, A. G. G. M., & van Dishoeck, E. F. 2005, MNRAS, 356, 1283
Garrod, R. T., Jin, M., Matis, K. A., et al. 2022, ApJS, 259, 1
Garrod, R. T., Widicus Weaver, S. L., & Herbst, E. 2008, ApJ, 682, 283
Gerakines, P. A. & Hudson, R. L. 2020, ApJ, 901, 52
Gerakines, P. A., Whittet, D. C. B., Ehrenfreund, P., et al. 1999, ApJ, 522, 357
Gerakines, P. A., Yarnall, Y. Y., & Hudson, R. L. 2022, MNRAS, 509, 3515
Gibb, E. L., Whittet, D. C. B., Boogert, A. C. A., & Tielens, A. G. G. M. 2004, ApJS, 151, 35
Gibb, E. L., Whittet, D. C. B., Schutte, W. A., et al. 2000, ApJ, 536, 347
Grim, R. J. A., Baas, F., Geballe, T. R., Greenberg, J. M., & Schutte, W. A. 1991, A&A, 243, 473
Herbst, E. & van Dishoeck, E. F. 2009, ARA&A, 47, 427
Huntress, W. T., J. & Mitchell, G. F. 1979, ApJ, 231, 456
Ioppolo, S., Fedoseev, G., Chuang, K. J., et al. 2021, Nature Astronomy, 5, 197
Jakobsen, P., Ferruit, P., Alves de Oliveira, C., et al. 2022, A&A, 661, A80
Jiménez-Escobar, A., Giuliano, B. M., Muñoz Caro, G. M., Cernicharo, J., & Marcelino, N. 2014, ApJ, 788, 19
Jiménez-Serra, I., Vasyunin, A. I., Caselli, P., et al. 2016, ApJ, 830, L6
Johnston, K. G., Keto, E., Robitaille, T. P., & Wood, K. 2011, MNRAS, 415, 2953

Jørgensen, J. K., Belloche, A., & Garrod, R. T. 2020, ARA&A, 58, 727
Jørgensen, J. K., Müller, H. S. P., Calcutt, H., et al. 2018, A&A, 620, A170
Jørgensen, J. K., van der Wiel, M. H. D., Coutens, A., et al. 2016, A&A, 595, A117
Keane, J. V., Tielens, A. G. G. M., Boogert, A. C. A., Schutte, W. A., & Whittet, D. C. B. 2001, A&A, 376, 254
Le Gal, R., Brady, M. T., Öberg, K. I., Roueff, E., & Le Petit, F. 2019, ApJ, 886, 86
Lee, C.-F., Li, Z.-Y., Ho, P. T. P., et al. 2017, ApJ, 843, 27
Ligterink, N. F. W. & Minissale, M. 2023, A&A, 676, A80
Ligterink, N. F. W., Terwisscha van Scheltinga, J., Taquet, V., et al. 2018, MNRAS, 480, 3628
Martín-Doménech, R., Bergner, J. B., Öberg, K. I., et al. 2021, ApJ, 923, 155
Maté, B., Herrero, V. J., Rodríguez-Lazcano, Y., et al. 2012, ApJ, 759, 90
McClure, M. K., Rocha, W. R. M., Pontoppidan, K. M., et al. 2023, Nature Astronomy, 7, 431
Meinert, C., Myrgorodska, I., de Marcellus, P., et al. 2016, Science, 352, 208
Minissale, M., Aikawa, Y., Bergin, E., et al. 2022, ACS Earth and Space Chemistry, 6, 597
Moore, M. H., Ferrante, R. F., Moore, W. J., & Hudson, R. 2010, ApJS, 191, 96
Muñoz Caro, G. M., Ciaravella, A., Jiménez-Escobar, A., et al. 2019, ACS Earth and Space Chemistry, 3, 2138
Narang, M., Manoj, P., Tyagi, H., et al. 2023, arXiv e-prints, arXiv:2310.14061
Nazari, P., Meijerhof, J. D., van Gelder, M. L., et al. 2022, A&A, 668, A109
Nazari, P., Tabone, B., Rosotti, G. P., & van Dishoeck, E. F. 2023a, Submitted to A&A
Nazari, P., Tabone, B., van 't Hoff, M. L. R., Jørgensen, J. K., & van Dishoeck, E. F. 2023b, ApJ, 951, L38
Nazari, P., van Gelder, M. L., van Dishoeck, E. F., et al. 2021, A&A, 650, A150
Novozamsky, J. H., Schutte, W. A., & Keane, J. V. 2001, A&A, 379, 588
Öberg, K. I., Boogert, A. C. A., Pontoppidan, K. M., et al. 2008, ApJ, 678, 1032
Öberg, K. I., Boogert, A. C. A., Pontoppidan, K. M., et al. 2011, ApJ, 740, 109
Öberg, K. I., Bottinelli, S., & van Dishoeck, E. F. 2009a, A&A, 494, L13
Öberg, K. I., Garrod, R. T., van Dishoeck, E. F., & Linnartz, H. 2009b, A&A, 504, 891
Öberg, K. I., Guzmán, V. V., Furuya, K., et al. 2015, Nature, 520, 198
Ortiz-León, G. N., Loinard, L., Dzib, S. A., et al. 2018, ApJ, 869, L33
Palumbo, M. E., Tielens, A. G. G. M., & Tokunaga, A. T. 1995, ApJ, 449, 674
Penteado, E. M., Walsh, C., & Cuppen, H. M. 2017, ApJ, 844, 71
Poch, O., Istiqomah, I., Quirico, E., et al. 2020, Science, 367, aaw7462
Pontoppidan, K. M., Boogert, A. C. A., Fraser, H. J., et al. 2008, ApJ, 678, 1005
Pontoppidan, K. M., Fraser, H. J., Dartois, E., et al. 2003, A&A, 408, 981
Pontoppidan, K. M., Salyk, C., Bergin, E. A., et al. 2014, in Protostars and Planets VI, ed. H. Beuther, R. S. Klessen, C. P. Dullemond, & T. Henning, 363–385
Qasim, D., Fedoseev, G., Chuang, K. J., et al. 2019, A&A, 627, A1
Rachid, M. G., Rocha, W. R. M., & Linnartz, H. 2022, A&A, 665, A89
Reid, M. J., Menten, K. M., Brunthaler, A., et al. 2019, ApJ, 885, 131
Rocha, W. R. M., Perotti, G., Kristensen, L. E., & Jørgensen, J. K. 2021, A&A, 654, A158
Rocha, W. R. M., Rachid, M. G., Olsthoorn, B., et al. 2022, A&A, 668, A63
Rocha, W. R. M., van Dishoeck, E. F., Ressler, M. E., et al. 2023, arXiv e-prints, arXiv:2312.06834
Roser, J. E., Ricca, A., Cartwright, R. J., Dalle Ore, C., & Cruikshank, D. P. 2021, PSJ, 2, 240
Ruaud, M., Wakelam, V., & Hersant, F. 2016, MNRAS, 459, 3756
Rubin, M., Altwegg, K., Balsiger, H., et al. 2019, MNRAS, 489, 594
Rubinstein, A. E., Tyagi, H., Nazari, P., et al. 2023, arXiv e-prints, arXiv:2312.07807
Russo, N. D. & Khanna, R. K. 1996, Icarus, 123, 366
Santos, J. C., Chuang, K.-J., Lamberts, T., et al. 2022, ApJ, 931, L33
Schutte, W. A., Boogert, A. C. A., Tielens, A. G. G. M., et al. 1999, A&A, 343, 966
Schutte, W. A. & Khanna, R. K. 2003, A&A, 398, 1049
Slavicinska, K., Gomes Rachid, M., Robson Monteiro Rocha, W., et al. 2023, arXiv e-prints, arXiv:2307.04790
Soifer, B. T., Puetter, R. C., Russell, R. W., et al. 1979, ApJ, 232, L53
Taniguchi, K., Sanhueza, P., Olguin, F. A., et al. 2023, arXiv e-prints, arXiv:2304.00267
Tobin, J. J., Sheehan, P. D., Megeath, S. T., et al. 2020, ApJ, 890, 130
van Broekhuizen, F. A., Keane, J. V., & Schutte, W. A. 2004, A&A, 415, 425
van Broekhuizen, F. A., Pontoppidan, K. M., Fraser, H. J., & van Dishoeck, E. F. 2005, A&A, 441, 249
van Dishoeck, E. F., Blake, G. A., Jansen, D. J., & Groesbeck, T. D. 1995, ApJ, 447, 760
van Dishoeck, E. F., Grant, S., Tabone, B., et al. 2023, arXiv e-prints, arXiv:2307.11817
van Gelder, M. L., Jaspers, J., Nazari, P., et al. 2022, A&A, 667, A136
van Gelder, M. L., Tabone, B., Tychoniec, Ł., et al. 2020, A&A, 639, A87
Vazart, F., Ceccarelli, C., Balucani, N., Bianchi, E., & Skouteris, D. 2020, MNRAS, 499, 5547
Walsh, C., Millar, T. J., Nomura, H., et al. 2014, A&A, 563, A33
Watson, D. M. 2020, Research Notes of the AAS, 4, 88
Wilner, D. J., Wright, M. C. H., & Plambeck, R. L. 1994, ApJ, 422, 642
Yang, Y.-L., Green, J. D., Pontoppidan, K. M., et al. 2022, ApJ, 941, L13
Yang, Y.-L., Sakai, N., Zhang, Y., et al. 2021, ApJ, 910, 20

Appendix A: Additional tables and plots

Table A.1 presents the centers of the apertures from which the spectra are extracted, in addition to the rms on the continuum optical depth and the source characteristics. Table A.2 presents the band strengths used for the column density measurements. Figure A.1 illustrates the positions from which the spectra are extracted in this work. Figure A.2 presents the local continuum fits to the extracted spectra. Figure A.3 presents the fit to the CN-stretching region for the emission-line-subtracted spectra (see Rubinstein et al. 2023). Figure A.4 is the same as Fig. 5 but for corrected gas-phase column density ratios. Figure A.5 presents the laboratory spectra of pure CH_3CN and C_2H_5CN to highlight the strongest features.
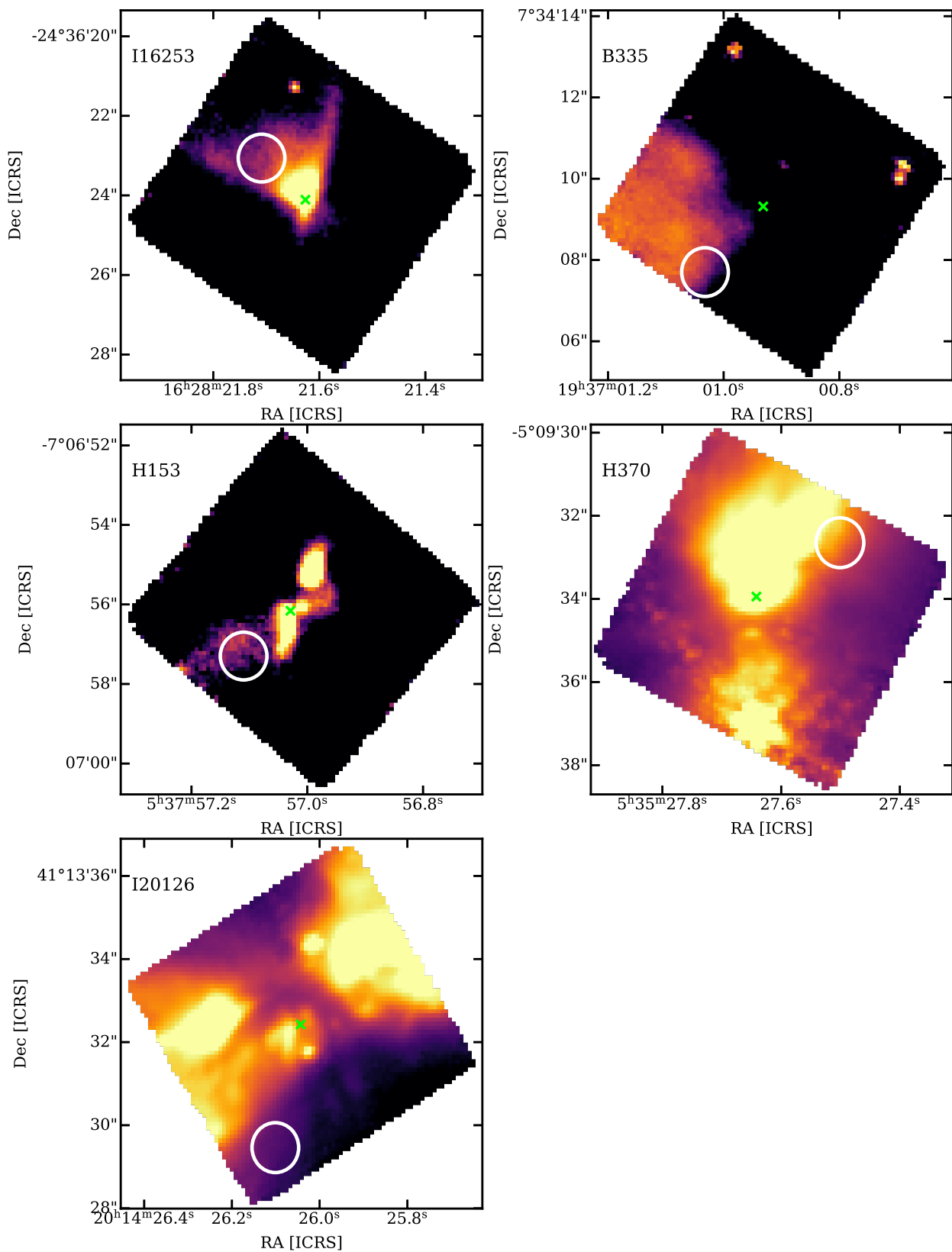
Fig. A.1: *JWST*-NIRSpec continuum images at $3.92\,\mu$m for the IPA targets. White circles show the apertures from which the spectra are extracted in this work to avoid the CO rotational-vibrational emission lines as much as possible. The central position of each protostar according to the IPA-MIRI channel 3 medium band is shown by a green cross.

Table A.1: Positions for spectral extraction and source properties

Source	R.A. [hh:mm:ss]	Decl. [dd:mm:ss]	Optical depth rms	L_{bol} [$L_\odot$]	d [pc]	References
IRAS 16253	16:28:21.71	-24:36:23.06	0.0045	0.16	140	Ortiz-León et al. (2018); Aso et al. (2023)
B335	19:37:01.03	07:34:07.70	0.014	1.4	165	Watson (2020); Evans et al. (2023)
HOPS 153	05:37:57.11	-07:06:57.30	0.0076	3.8	390	Tobin et al. (2020)
HOPS 370	05:35:27.50	-05:09:32.65	0.0009	315.7	390	Tobin et al. (2020)
IRAS 20126	20:14:26.10	41:13:29.46	0.0026	10^4	1550	Johnston et al. (2011); Reid et al. (2019)

Notes. Second and third column give the right ascension and declination of the center of the aperture used to extract the spectrum (see Fig. A.1). The references of bolometric luminosities and distances of the central sources are given in the right-most column.
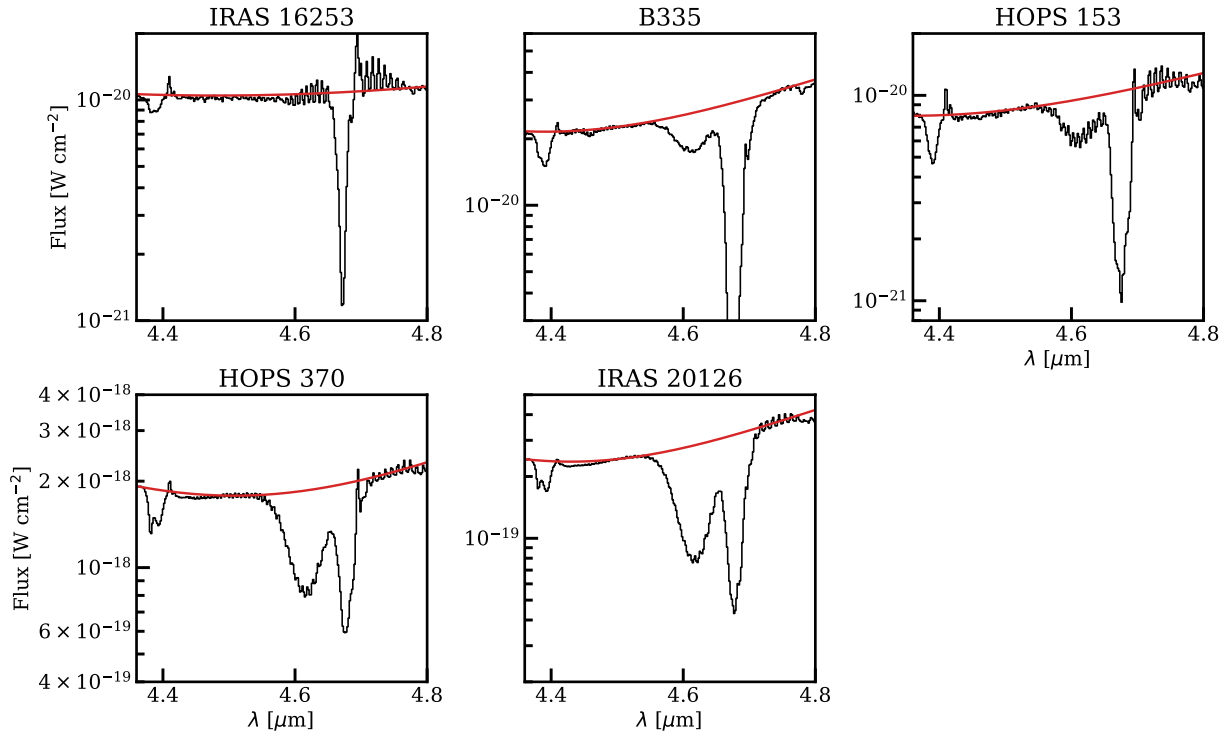

Fig. A.2: Spectra (black) and the fitted continuum (red) for all the five sources in the IPA program. The continuum is fitted locally using a polynomial function.

Table A.2: Band strengths

Ice species	A (cm molecule^{-1})
$CH_3CN:CO_2$	1.5×10^{-18}
$CH_3CN:CO$	1.5×10^{-18}
$CH_3CN:H_2O:CO_2$	3.3×10^{-18}
C_2H_5CN	2.9×10^{-18}
OCN^-	1.3×10^{-16}

Notes. The band strengths are taken from Rachid et al. (2022) and van Broekhuizen et al. (2004) for CH_3CN mixtures and OCN^-, respectively, while they are calculated for C_2H_5CN in this work.
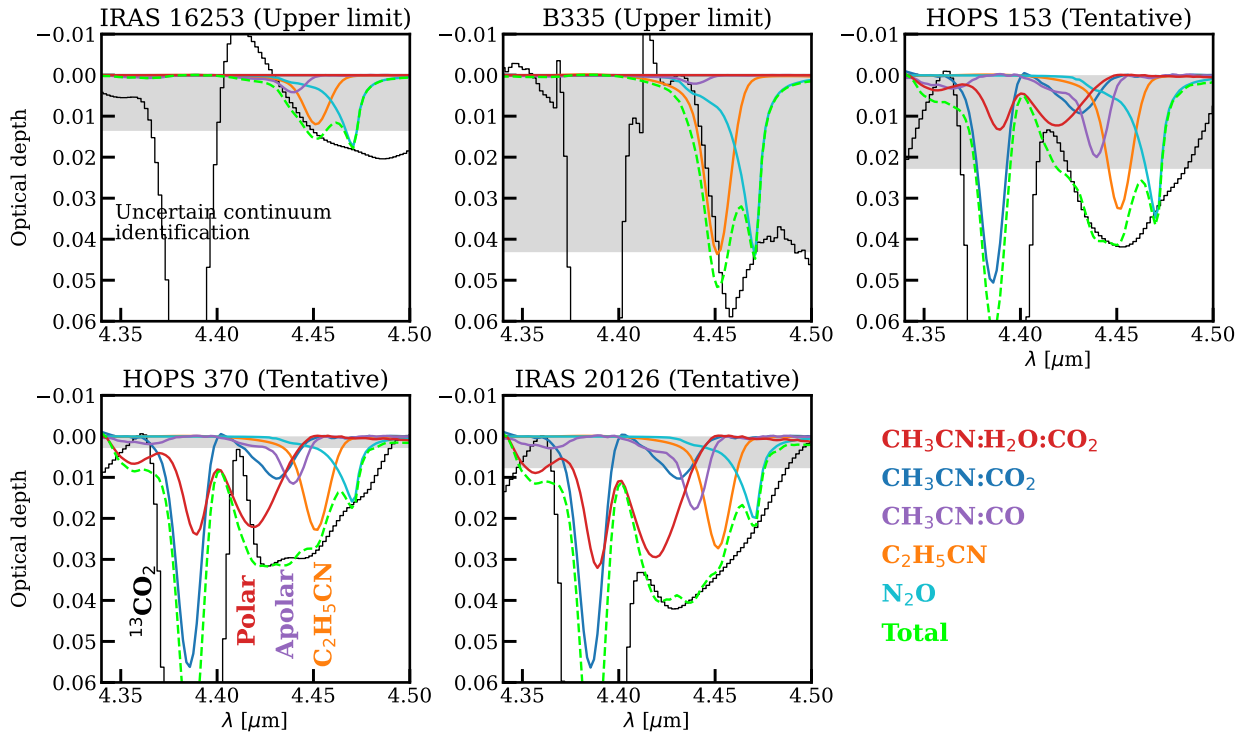
Fig. A.3: Same as Fig. 3 but for the emission-line-subtracted spectra taken from Rubinstein et al. (2023) where the methods of emission line fitting and subtraction are explained.
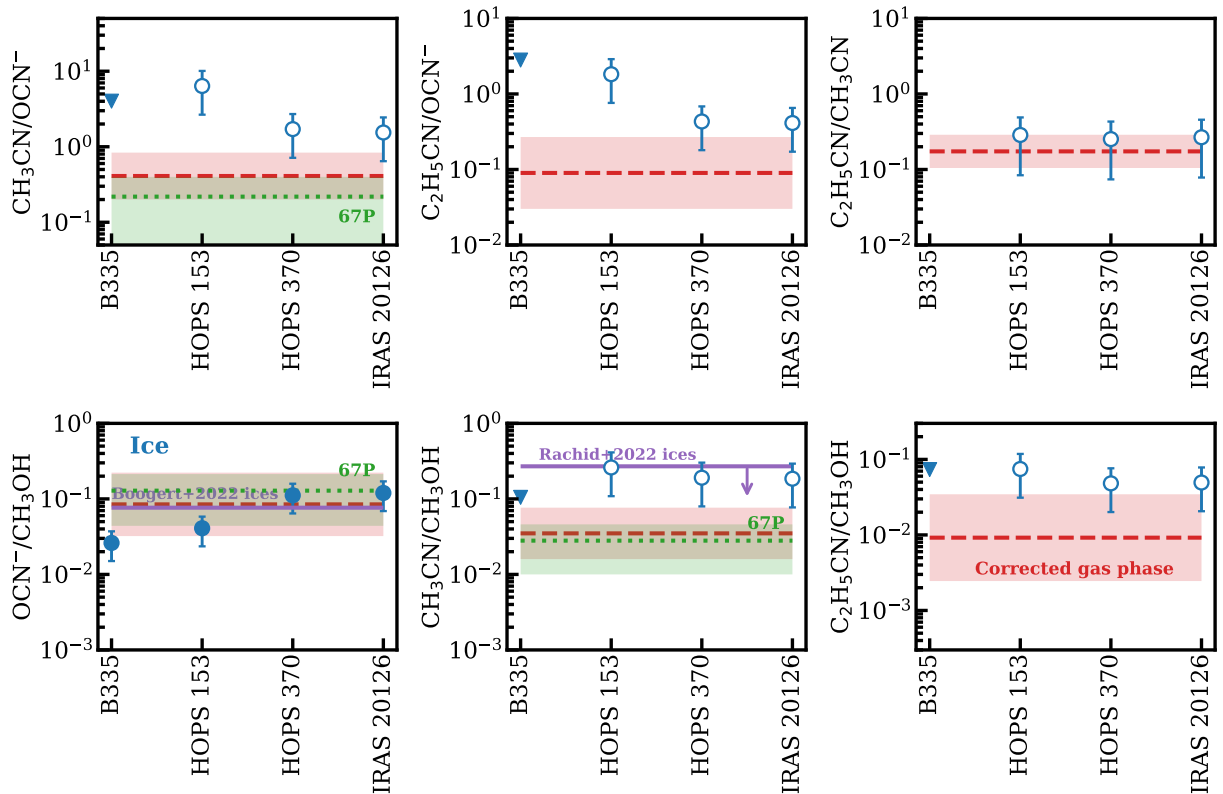

Fig. A.4: Same as Fig. 5 but now the gas-phase column density ratios are corrected by a factor of 4.6 for potential differences between the snowline locations of nitrogen-bearing molecules with respect to methanol.
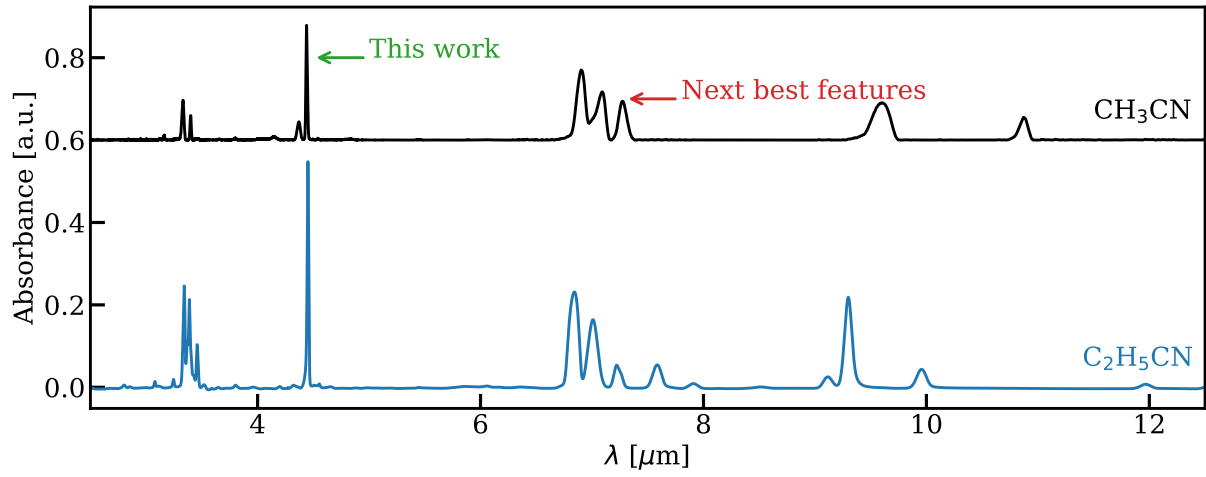
Fig. A.5: Laboratory spectra of pure CH$_3$CN and C$_2$H$_5$CN at 15 K and 50 K, respectively, to highlight which feature can be used in the future for firm detection of these two species. The spectrum of CH$_3$CN is shifted vertically for better readability.